



Interpreting Solar Wind Turbulent Spectra beyond Taylor's Hypothesis

Sofiane Bourouaine and Jean C. Perez

Florida Institute of Technology, 150 W University Boulevard, Melbourne, FL 32901, USA; sbourouaine@fit.edu

Received 2020 January 22; revised 2020 March 12; accepted 2020 March 12; published 2020 April 20

Abstract

In this Letter we apply a methodology, recently proposed by Bourouaine & Perez (BP19), to interpret solar wind turbulent power spectra beyond the Taylor approximation (TA). The turbulent power spectra were measured using Helios spacecraft data near 0.6 au. We use the model proposed in BP19 to reproduce the field-perpendicular power spectrum $E(k_{\perp})$ of antisunward Alfvénic fluctuations in the plasma frame (where k_{\perp} is the field-perpendicular wavenumber) from the corresponding measured frequency power spectrum $P_{sc}(\omega, \theta_b)$ along the sampling angle θ_b , which is the angle between the local magnetic field and the sampling direction. Here $\omega = 2\pi f$ and f is the frequency of the time signal. Interestingly enough, we found that for all corresponding measured frequency power spectrum $P_{sc}(\omega, \theta_b)$ the reproduced field-perpendicular power spectrum $E(k_{\perp})$ is the same and independent of the considered sampling angle θ_b . This finding is consistent with the fact that the analyzed turbulence is strong and highly anisotropic with $k_{\parallel} \ll k_{\perp}$ (where k_{\parallel} is the field-parallel wavenumber). Furthermore, for this specific time signal we found that the commonly used TA is still approximately valid with the important difference that a broadening in k_{\perp} for each angular frequency ω is present. This broadening can be described in the context of the methodology proposed in BP19.

Unified Astronomy Thesaurus concepts: [Solar magnetic fields \(1503\)](#); [Fast solar wind \(1872\)](#); [Interplanetary turbulence \(830\)](#); [Alfvén waves \(23\)](#); [Space plasmas \(1544\)](#)

1. Introduction

Most analyses of solar wind observations normally adopt the Taylor approximation (TA), often called Taylor's hypothesis (TH; Taylor 1938), to investigate turbulent time signals from in situ spacecraft measurements, and thus study the fundamental physics of solar wind turbulence. TH assumes that when the turbulent fluctuations are advected with a speed U that is much higher than the typical fluctuation speed v ($U \gg v$), the time (τ) and the spatial (r) lags of the measured structures are connected as $r = U\tau$. However, this frozen-in-flow approximation may not be applicable in all solar wind conditions, most importantly at heliocentric distances where the recently launched Parker Solar Probe (PSP; Fox et al. 2016) mission is expected to explore (see, for instance, Bourouaine & Perez 2018, hereafter BP18).

Recently, with the new PSP mission there has been an increased and renewed interest in investigating the applicability of the TH in the solar wind (Klein et al. 2014, 2015; Narita 2017; Bourouaine & Perez 2018, 2019; Chhiber et al. 2019; Huang & Sahraoui 2019). More recently, Bourouaine & Perez (2019, hereafter BP19) proposed a phenomenological model to explain the time decorrelation of the turbulent structures by extending Kraichnan's hydrodynamic sweeping model to MHD turbulence. The form of the temporal part of the two-point two-time correlation function in the BP19 model allows for the interpretation of the turbulent time signal even when $v \sim U$ and TH is not valid.

The fundamental physics of the time decorrelation of MHD turbulent structures has been investigated in a number of previous works (Matthaeus et al. 2010, 2016; Servidio et al. 2011; Narita et al. 2013; Narita 2017; Weygand et al. 2013). For instance, BP19 found that the Eulerian decorrelation in simulations is consistent with spectral broadening associated with pure hydrodynamic sweeping by the large-scale eddies, combined with a Doppler shift associated with Alfvénic

propagation along the background magnetic field in strong MHD turbulence.

In this Letter we present a practical application of the model proposed in BP19 to reproduce the reduced energy spectrum in the plasma frame beyond the TA. For this purpose we analyze turbulent signals measured by Helios 2 near 0.6 au. In Section 2 we calculate the power spectra of the antisunward propagating Elsässer field and the fluid velocity field in the spacecraft frame through the correlations functions. In Section 3, we reproduce the reduced field-perpendicular power spectrum and the broadening in the field-perpendicular wavenumber k_{\perp} , using the model proposed in BP19, and then using the TA. Finally, we summarize and discuss the obtained results in Section 4.

2. Data and Methodology

In our analysis we use combined plasma-field data provided by Helios 2 with a time resolution of about 40.5 s. We focus on the analysis of plasma and magnetic field signals measured within the time period 1976 March 15 (00:00:30.00) to 1976 March 18 (22:58:12.00). During this time period the spacecraft is passing mostly through fast solar wind as we can see in Figure 1.

In this analysis we aim to reproduce the reduced energy spectrum $E(k_{\perp}) = 2\pi k_{\perp} \int h_0(k_{\parallel}, k_{\perp}) dk_{\parallel}$ in the inertial range. Here $h_0(k_{\parallel}, k_{\perp})$ is the plasma-frame three-dimensional power spectrum corresponding to the antisunward propagating Elsässer field $\delta z^{-} = \delta v - \delta \mathbf{b} / \sqrt{4\pi\rho}$, where δv is the fluctuating bulk velocity vector, $\delta \mathbf{b}$ is the fluctuating magnetic field vector, and ρ is the proton mass density. We define the local mean magnetic and velocity vectors as the moving average over a period T around time t_j , i.e.,

$$\mathbf{B}_0(t_j) = \frac{1}{N_j} \sum_i W_T(t_j - t_i) \mathbf{b}(t_i), \quad (1)$$

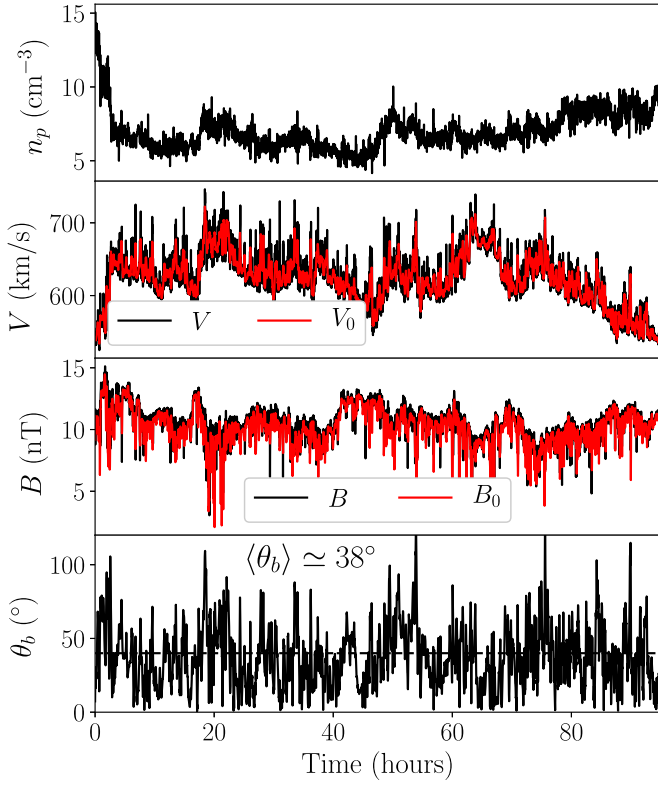


Figure 1. Time period of the signal is from 1976 March 15 (00:00:30.00) to 1976 March 18 (22:58:12.00) near 0.6 au. Top panel: proton number density. Middle top panel: solar wind speed V (black line) and local mean speed V_0 as defined in Equation (2) (red line). Middle bottom panel: magnetic field magnitude B (black line) and local mean field B_0 as defined by Equation (1) (red line). Bottom panel: sampling angle θ_b between vectors V_0 and B_0 . All signals are plotted as functions of time t .

$$V_0(t_j) = \frac{1}{N_j} \sum_i W_T(t_j - t_i) \mathbf{v}(t_i), \quad (2)$$

where N_j is the number of averaging samples and $W_T(t)$ is a windowing function that vanishes everywhere except at $|t| \leq T/2$, in which case it is equal to one. The period $T \simeq 9$ minutes is chosen to be close to the corresponding time decorrelation for which the value of the normalized correlation function is less than 0.2 (Figure 2). The magnitudes of the local mean velocity and local magnetic field are shown as red lines in Figure 1. The corresponding angle $\theta_b(t)$ between the two vectors $V_0(t)$ and $B_0(t)$ is plotted as a function of time t in the bottom panel of Figure 1.

In the following analysis we estimate the power spectra $P_{sc}(\omega, \theta_i)$ and $P_{sc}^v(\omega, \theta_i)$ that correspond to \mathbf{z}^- and \mathbf{v} , respectively, along a sampling angle $\theta_b \simeq \theta_i$, where θ_i are the angle bins of width $\Delta\theta = 10^\circ$ centered at the following angle values $\theta_0 = 20^\circ$, $\theta_1 = 30^\circ$, $\theta_2 = 40^\circ$, $\theta_3 = 50^\circ$, and $\theta_4 = 60^\circ$.

Generally, the power spectrum of a fluctuating vector quantity $\mathbf{a}(t)$ can be obtained through the Fourier transform of its autocorrelation function $C(\tau) = \langle \mathbf{a}(t_0) \cdot \mathbf{a}(t_0 + \tau) \rangle$ (see, e.g., Bourouaine & Chandran 2013), where τ is the time lag. In our analysis, the empirical power spectra $P_{sc}(\omega, \theta_i)$ and $P_{sc}^v(\omega, \theta_i)$ are then obtained as the Fourier transform of the following conditioned correlation functions:

$$C_v(\tau, \theta_i) = \langle (\mathbf{v}(t) - \bar{\mathbf{v}}) \cdot (\mathbf{v}(t + \tau) - \bar{\mathbf{v}}) \rangle_{\theta_i, V_0, R}, \quad (3)$$

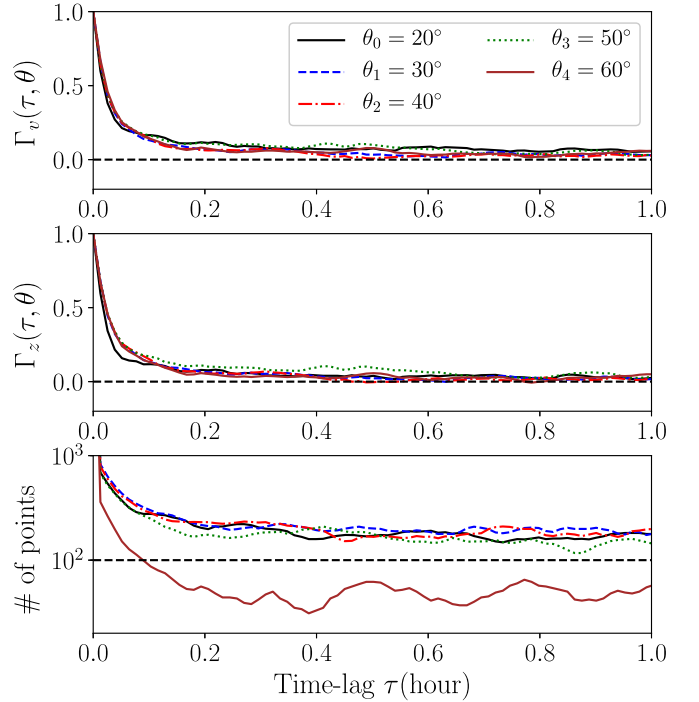


Figure 2. Normalized correlation functions $\Gamma_v(\tau, \theta_i)$ (top) and $\Gamma_z(\tau, \theta)$ (middle) for different θ_i . The bottom panel shows the number of points used in the statistical ensemble average of the correlation functions for given time-lag τ . All plotted for different binned values of θ_i .

$$C_z(\tau, \theta_i) = \langle (\mathbf{z}^-(t) - \bar{\mathbf{z}}^-) \cdot (\mathbf{z}^-(t + \tau) - \bar{\mathbf{z}}^-) \rangle_{\theta_i, V_0, R}, \quad (4)$$

where $\langle \dots \rangle_{\theta_i, V_0, R}$ denotes the ensemble average, computed over many realizations (or averaged over time t) conditioned by the angle bin θ_i , mean velocity V_0 , and the transverse ratio $R = (\delta z_{\parallel}^- / \delta z_{\perp}^-)^2$. Here, the perpendicular and the parallel components of the fluctuations $\delta \mathbf{z}^-$ are defined with respect to the local mean magnetic field B_0 . As we are interested in fast solar wind and transverse fluctuations, we calculate correlation functions by considering only the statistics of those two times t and $t + \tau$ in Equations (3) and (4) for which the corresponding values of the mean velocity $V_0 \geq 600 \text{ km s}^{-1}$ and the ratio $R < 0.2$. $\bar{\mathbf{v}}$ and $\bar{\mathbf{z}}^-$ were obtained through averaging over all considered points in the calculation of the correlation functions.

Note that the correlation functions in Equations (3) and (4) are calculated using global mean vectors $\bar{\mathbf{v}}$ and $\bar{\mathbf{z}}^-$ instead of local mean vectors V_0 and B_0 , respectively. This is done in order to capture the frequency power spectrum of the outer scale (i.e., scales that are larger than period T), which then allows us to properly estimate the rms speed of the energy-containing eddies required for the reproduction of the reduced energy spectrum $E(k_{\perp})$ according to the BP19 model.

It is worth mentioning that there are two main advantages of calculating the power spectra through the correlation functions: (1) we can be selective and avoid any unwanted points, including gaps of bad measurements in the calculation of the correlation functions, and (2) we can check the statistics that correspond to the estimation of the correlation functions for each time-lag τ including the statistics of the outer scale for large τ .

Figure 2 shows the curves of the normalized correlation functions $\Gamma_v(\tau, \theta_i) = C_v(\tau, \theta_i) / C_v(0, \theta_i)$ and $\Gamma_z(\tau, \theta_i) = C_z(\tau, \theta_i) / C_z(0, \theta_i)$ as a function of time-lag τ . For all θ_i the

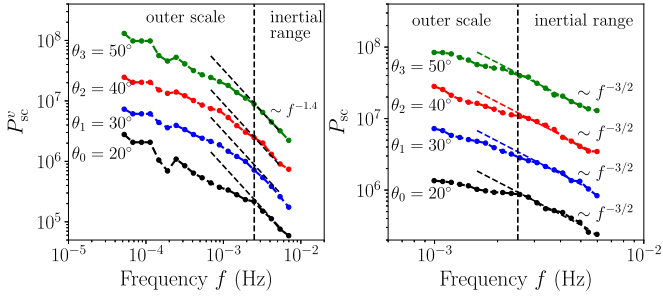


Figure 3. Spacecraft-frame power spectra for velocity $P_{sc}^v(\omega, \theta_i)$ (left panel) and for Elsasser field $z^-, P_{sc}(\omega, \theta_i)$ (right panel). All power spectra were plotted as a function of the frequency $f = \omega/(2\pi)$ measured in the spacecraft frame. All spectra were fitted to power-law functions within the frequency range $[2.5 \times 10^{-3}, 6 \times 10^{-3}]$ Hz (inertial range). The different curves have been offset vertically for easier viewing. We also excluded the part of the power spectra that is affected by noise for $f > 6 \times 10^{-3}$ Hz.

normalized correlations Γ_v and Γ_z drop sharply for $\tau \lesssim 12$ minutes, and they practically vanish when $\tau \gtrsim 30$ minutes. As shown in the bottom panel of Figure 2, all the correlations, except those corresponding to $\theta_4 = 60^\circ$, were measured with reasonably good statistics, with a minimum number of points higher than 100. Therefore, we do not consider the analysis for $\theta_4 = 60^\circ$ due to a lack of reliable statistics.

Figure 3 displays power spectra $P_{sc}^v(\omega, \theta_i)$ and $P_{sc}(\omega, \theta_i)$ computed through the Fourier transform of the corresponding correlation functions (Figure 2) for each angle bin θ_i . The four spectra in this figure have been artificially offset for easier viewing. We excluded the part of the power spectra (for $f \gtrsim 6 \times 10^{-3}$) that is affected by the noise due to the time resolution of the plasma experiment. Also, we plotted the very low frequency part only for the power spectra $P_{sc}^v(\omega, \theta_i)$ as we will use it to estimate the rms of the outer-scale bulk velocity.

The power spectrum $P_{sc}^v(\omega, \theta_i)$ seems to steepen for frequencies above $\sim 2.5 \times 10^{-3}$ Hz showing a spectral index of about -1.4 . The outer scale of the velocity field (frequency below $f_1 \sim 2.5 \times 10^{-3}$ Hz) follows a power law that is comparable to or steeper than f^{-1} . We estimate the value of the outer-scale rms bulk speed, $\delta u_{i,0}$, for each power spectrum $P_{sc}^v(\omega, \theta_i)$ as

$$\delta u_{i,0} = 4\pi \int_0^{f_1} P_{sc}^v(2\pi f, \theta_i) df. \quad (5)$$

The right panel of Figure 3 displays the power spectrum $P_{sc}(\omega, \theta_i)$ within the frequency range between 10^{-3} Hz and 10^{-2} Hz. The power spectra are fitted to power laws in the inertial range (within the frequency range $f \in [2.5 \times 10^{-3}, 6 \times 10^{-3}]$ Hz), of the form $P_{sc}(\omega, \theta_i) = D_i \omega^{-\alpha}$ for both $\alpha = 3/2$ and $\alpha = 5/3$. The values obtained for the energy constant D_i for each value of α are listed in Table 1.

3. The Reduced Spatial Power Spectrum

3.1. Derivation of $E(k_\perp)$ Using BP19 Model

We estimate a reduced energy spectrum $E(k_\perp)$ associated with each measured spacecraft-frame $P_{sc}(\omega, \theta_i)$. According to the BP19 model, for the strong turbulence case, the spectral index of the reduced power spectrum $E(k_\perp)$ in the inertial range will be the same as the spectral index of their corresponding frequency spectrum $P_{sc}(\omega, \theta_i)$; therefore, $E(k_\perp) = C_i k_\perp^{-\alpha}$ where C_i is expected to be the same constant for each sampling angle

Table 1
Relevant Measured Parameters Used to Reconstruct Power Spectrum $E(k_\perp)$ from the BP19 Model

i	0	1	2	3
θ_i	20°	30°	40°	50°
$V_{i,\perp}$ (km s $^{-1}$)	219	319	404	482
$D_i \times 10^{-8}$ (SI) ($\alpha = 5/3$)	1.5	2.2	2.3	2.7
$D_i \times 10^{-8}$ (SI) ($\alpha = 3/2$)	2.6	3.3	3.8	4.6
$\delta u_{i,0}$ (km s $^{-1}$)	32	38	41	43
ϵ_i	0.10	0.08	0.07	0.06
Λ_i ($\alpha = 5/3$)	0.71	0.71	0.71	0.71
Λ_{TA} ($\alpha = 5/3$)	0.71	0.71	0.71	0.71
$C_i \times 10^{-4}$ (SI) ($\alpha = 5/3$)	6.0	5.8	5.7	6.0
$C_i \times 10^{-5}$ (SI) ($\alpha = 3/2$)	6.0	6.0	6.2	6.7
$C_{i,TA} \times 10^{-4}$ (SI) ($\alpha = 5/3$)	6.0	5.8	5.7	6.0
$C_{i,TA} \times 10^{-5}$ (SI) ($\alpha = 3/2$)	6.0	6.0	6.2	6.7
$x_{i,0}$ ($\alpha = 5/3, 3/2$)	0.2	0.2	0.2	0.2
$x_{i,1}$ ($\alpha = 5/3, 3/2$)	1.1	1.1	1.0	1.0

Note. The mean Alfvén velocity $v_A = 80$ km s $^{-1}$.

θ_i if the turbulence is strong and highly anisotropic. From the BP19 model we have the following relationship:

$$P_{sc}(\omega, \theta_i) = \Lambda_i \frac{C_i}{V_{i,\perp}} \left(\frac{\omega}{V_{i,\perp}} \right)^{-\alpha}, \quad (6)$$

where

$$\Lambda_i = \int_0^\infty f_{\epsilon_i}(\alpha, x) dx, \quad (7)$$

$$f_{\epsilon_i}(\alpha, x) = x^{\alpha-1} \bar{g}_{\epsilon_i}(x), \quad (8)$$

and $\bar{g}_{\epsilon_i}(x)$ is a function of the dimensionless parameter $x = \omega/k_\perp V_{i,\perp}$ that is connected to the probability distribution g (y) of outer-scale velocities (assumed to be a Gaussian distribution) as follows:

$$\bar{g}_{\epsilon_i}(x) = \frac{2}{\pi} \int_0^\pi \frac{1}{\epsilon_i} g\left(\frac{x + \cos \phi}{\epsilon_i}\right) d\phi, \quad (9)$$

where

$$g(y) = \frac{1}{\sqrt{2\pi}} e^{-\frac{1}{2}y^2} \quad (10)$$

and the parameter $\epsilon_i = \delta u_{i,0}/(\sqrt{2} V_{i,\perp})$ with $V_{i,\perp} = \bar{V}_{i,0} \sin \theta_i$ is the field-perpendicular velocity of the spacecraft as seen in the plasma frame, and $\bar{V}_{i,0}$ is computed through averaging over all points of V_0 considered in the calculation of the correlation functions in Equations (3) and (4) for a given angle bin. All the empirical values of the above parameters are given in Table 1. The angle ϕ in Equation (9) is the direction of the wavevector \mathbf{k}_\perp in the field-perpendicular plane. By replacing the power-law fits $P_{sc}(\omega, \theta_i) = D_i \omega^{-\alpha}$ in Equation (6), we get

$$C_i = \frac{D_i}{\Lambda_i} V_{i,\perp}^{-\alpha+1}. \quad (11)$$

Equation (11) can now be used to find the values of C_i , summarized Table 1, that correspond to the reduced power spectra $E(k_\perp)$ in the inertial range. Interestingly, the values of C_i are all around 6×10^5 (6×10^4) in SI units for $\alpha = 3/2$ ($\alpha = 5/3$), and there is no dependency on the sampling angle

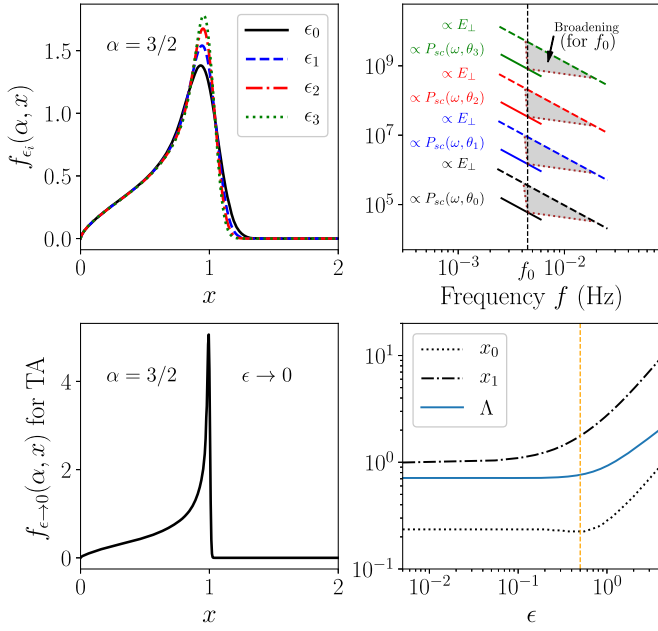


Figure 4. Top left: the functions $f_{\epsilon_i}(\alpha, x)$ plotted as a function of the dimensionless variable x for the empirical values of ϵ_i and $\alpha = 3/2$. Top right: part of the inertial-range power-law fits $\propto D_i(2\pi f)^{-\alpha}$ (colored solid lines) that correspond to $P_{sc}(\omega, \theta_i)$. The dashed colored lines are the corresponding reduced power spectra $\propto C_i f^{-\alpha}$ (where $f = k_{\perp} V_{i,\perp}/(2\pi)$). The different power-law curves have been offset vertically for easier viewing. The broadening in k_{\perp} that corresponds to frequency $f_0 = 4.5 \times 10^{-3}$ Hz is shown in the frequency-domain interval (gray areas) as $[k_{i,\min}, k_{i,\max}] V_{i,\perp}/(2\pi) = [f_0/x_{i,1}, f_0/x_{i,0}] \simeq [f_0/0.2, f_0/1.1]$ (see Equation (14)). Bottom left: curves represent the function $f_{\epsilon \rightarrow 0}(\alpha, x)$ plotted for $\alpha = 3/2$. Bottom right: curves of Λ (solid line), x_0 (dot line), and x_1 (dash line) plotted vs. ϵ all estimated for $\alpha = 3/2$.

θ_i . This is a strong signature that the turbulence is strong and anisotropic as found in many previous works (Horbury et al. 2008; Podesta 2009; Chen et al. 2011).

The top left panel of Figure 4 displays the function $f_{\epsilon_i}(\alpha, x)$ for the empirical parameters ϵ_i . The values of Λ_i were obtained through Equation (7) and summarized in Table 1. The curves of $f_{\epsilon_i}(\alpha, x)$ are seen to be broad in $x = \omega/k_{\perp} V_{i,\perp}$. According to BP19, TA can be recovered when $\epsilon \ll 1$ and its accuracy worsens when the broadening of $f_{\epsilon_i}(\alpha, x)$ becomes significant, as we discuss in the next subsection. The broadening in x will basically lead to broadening in the field-perpendicular wavenumber k_{\perp} . This means that the energy $P_{sc}(\omega, \theta_i)$ at a small frequency bin around ω corresponds to the energy in the wavenumber range $\Delta k_{i,\perp} = [k_{i,\min}, k_{i,\max}]$ according to the energy power $E(k_{\perp})$. This broadening can be determined from the broadening $\Delta x_i = [x_{i,0}, x_{i,1}]$ of the function $f_{\epsilon_i}(\alpha, x)$. The values of $x_{i,0}$ and $x_{i,1}$ can be estimated from the following two prescriptions: (1) the integral

$$\int_{x_{i,0}}^{x_{i,1}} f_{\epsilon_i}(\alpha, x) dx = \eta \Lambda_i \quad (12)$$

captures a desired fraction (e.g., $\eta \simeq 0.9$) of the Λ_i parameter, and (2)

$$\int_{x_{i,0}}^0 f_{\epsilon_i}(\alpha, x) dx = \int_{x_{i,1}}^{\infty} f_{\epsilon_i}(\alpha, x) dx. \quad (13)$$

With this prescription one then obtains the broadening in k_{\perp} for each frequency as

$$k_{i,\min} = \omega/(x_{i,1} V_{i,\perp}) \quad \text{and} \quad k_{i,\max} = \omega/(x_{i,0} V_{i,\perp}) \quad (14)$$

corresponding to each power spectrum $P_{i,sc}(\omega, \theta_i)$. Using $\eta = 0.90$ in this analysis leads to the values of $x_{i,0}$ and $x_{i,1}$ summarized in Table 1. For all considered θ_i , the broadening seems to be the same for the empirical values of $\epsilon_i \lesssim 0.1$.

In the top right panel of Figure 4 we illustrate¹ the broadening in k_{\perp} that contributes to the power spectrum $P_{sc}(\omega_0, \theta_i)$ for frequency $\omega_0 = 2\pi f_0$, where $f_0 = 4.5 \times 10^{-3}$ Hz. It is worth mentioning that the methodology proposed in BP19 can be used to reconstruct the reduced energy spectrum as long as $\tan \theta_b \gtrsim \delta u_0/v_A$, i.e., $\tan \theta_b \gtrsim 20^\circ$ for the data set considered in this work.

3.2. Derivation of $E(k_{\perp})$ Using the Taylor Approximation

As suggested in the BP19 sweeping model, the TA can be recovered in the limit when $\epsilon \rightarrow 0$. It is straightforward to show from Equation (9)

$$\lim_{\epsilon \rightarrow 0} \bar{g}_{\epsilon}(x) = \begin{cases} \frac{2}{\pi \sqrt{1-x^2}} & 0 < x < 1 \\ 0 & \text{otherwise} \end{cases}, \quad (15)$$

from where it follows that using Equations (7) and (8)

$$\Lambda_{TA} = \frac{2}{\pi} \int_0^1 \frac{x^{\alpha-1}}{\sqrt{1-x^2}} dx = \frac{\Gamma(\frac{\alpha}{2})}{\sqrt{\pi} \Gamma(\frac{\alpha+1}{2})}, \quad (16)$$

where $\Gamma(x)$ is the Gamma function. Thus the relationship that connects the reduced power spectrum $E(k_{\perp}) \simeq C_{i,TA} k_{\perp}^{-\alpha}$ and the spacecraft-frame power spectrum $P_{sc}(\omega, \theta_i)$ given in Equation (6) will become

$$P_{sc}(\omega) = \Lambda_{TA} \frac{C_{i,TA}}{V_{i,\perp}} \left(\frac{\omega}{V_{i,\perp}} \right)^{-\alpha}. \quad (17)$$

The values of Λ_{TA} and the corresponding energy constants $C_{i,TA}$ for the spectral indices $\alpha = 3/2$ and $5/3$ are listed in Table 1. The results from this analysis show that for $C_i \simeq C_{i,TA}$ in SI units (and $\Lambda_i \simeq \Lambda_{TA}$) for both values of α , suggesting that the TA is still a good approximation for empirical values of $\epsilon_i \lesssim 0.1$. The function $f_{\epsilon \rightarrow 0}(\alpha = 3/2, x)$ that is used to compute $\bar{g}_{\epsilon \rightarrow 0}(x)$ in Equation (15) in TA are plotted in the bottom left panel of Figure 4. Even when $\epsilon \ll 1$ (TA) there is still some broadening that is caused by the integration over angle ϕ . The estimation of the broadening in x for the TA case provide the same values of $x_{i,0}$ and $x_{i,1}$ as found using the BP19 methodology.

The analysis we present suggests that the BP19 model and TA provide a similar prediction for the energy constant. However, the TA obtained from BP19 in the limit of $\epsilon \rightarrow 0$ takes into account the broadening in k_{\perp} for a corresponding angular frequency ω , which arises from the angular integration of the wavevector in the field-perpendicular plane. To the best of our knowledge, the effect of this broadening within TA approximation has not been taken into account in solar wind observations. As our results show, for observations with $\epsilon \lesssim 0.1$, both the energy constant and broadening are the same as with the TA. For larger values of ϵ , this is not necessarily the case. For instance, in the bottom right panel of Figure 4 we estimate the parameter Λ and the corresponding values of x_0 and x_1 assuming $\alpha = 3/2$ and varying ϵ from 10^{-3} to 4. Interestingly, the parameter Λ remains roughly constant for

¹ In the figure we rescaled $E(k_{\perp})$ by various factors for clarity.

$\epsilon \lesssim 0.5$, which means that we would expect the same values for the energy constant whether applying the BP19 model or TA for this range of ϵ . The parameter Λ begins to change appreciably when $\epsilon \gtrsim 0.5$. This value of $\epsilon \gtrsim 0.5$ might be obtained near the Sun region when dealing with time signals near the Sun region where PSP is going to explore. The broadening seems to not change dramatically when $\epsilon \lesssim 0.1$; however, when $\epsilon > 0.1$ the curves of x_0 and x_1 begin to change. We conclude that for $\epsilon \lesssim 0.1$ both TA and BP19 lead to the same energy constant and broadening, for $0.1 \lesssim \epsilon \lesssim 0.5$ the TA properly captures the energy constant but not the broadening, while for any value of $\epsilon > 0.5$ the TA can no longer be justified.

4. Conclusion

In this analysis we applied the methodology proposed recently by BP19 to reproduce the reduced power spectra $E(k_{\perp})$ in the inertial range (in the plasma frame of reference) from the empirically measured power spectra $P_{sc}(\omega, \theta_i)$ for each binned angle θ_i . The values of the constants C_i seem to be independent of the sampling angle θ_i . This conclusion is clearly consistent with the fact that the studied turbulence is strongly anisotropic. Interestingly, we found that, when $\epsilon \lesssim 0.1$, the estimated energy constant C_i from the BP19 model is comparable to the one obtained through TA, but at any value of ϵ , including when $\epsilon \rightarrow 0$ (for TA), there will always be a significant broadening in k_{\perp} associated with a given frequency ω . The broadening in k_{\perp} that appears when $\epsilon \rightarrow 0$ is due to the integration over the ϕ angle. Many previous works considered the integration over ϕ using TA in the estimation of the energy spectrum $E(k_{\perp})$ (e.g., Bourouaine & Chandran 2013; Vech et al. 2017; Martinović et al. 2019). Broadening due to sweeping of the large scale will be more significant as ϵ increases. The application of the BP19 model provides a significant difference in the evaluation of the energy constant C than when TA is used if ϵ is larger than 0.5, which may very well occur in the solar wind, namely, near the Sun region where PSP is expected to explore.

S.B. was supported by NASA grants NNX16AH92G, 80NSSC19K0275 and 80NSSC19K1390. J.C.P. was partially supported by NASA grants NNX16AH92G, 80NSSC19K0275 and NSF grant AGS-1752827. The authors would also like to acknowledge constructive discussions with Kristopher Klein, Mihailo Martinović, and Christopher Chen.

ORCID iDs

Sofiane Bourouaine  <https://orcid.org/0000-0002-2358-6628>
Jean C. Perez  <https://orcid.org/0000-0002-8841-6443>

References

- Bourouaine, S., & Chandran, B. D. G. 2013, *ApJ*, 774, 96
 Bourouaine, S., & Perez, J. C. 2018, *ApJL*, 858, L20
 Bourouaine, S., & Perez, J. C. 2019, *ApJL*, 879, L16
 Chen, C. H. K., Mallet, A., Yousef, T. A., Schekochihin, A. A., & Horbury, T. S. 2011, *MNRAS*, 415, 3219
 Chhiber, R., Usmanov, A. V., Matthaeus, W. H., Parashar, T. N., & Goldstein, M. L. 2019, *ApJS*, 242, 12
 Fox, N. J., Velli, M. C., Bale, S. D., et al. 2016, *SSRv*, 204, 7
 Horbury, T. S., Forman, M., & Oughton, S. 2008, *PhRvL*, 101, 175005
 Huang, S. Y., & Sahraoui, F. 2019, *ApJ*, 876, 138
 Klein, K. G., Howes, G. G., & TenBarge, J. M. 2014, *ApJL*, 790, L20
 Klein, K. G., Perez, J. C., Verscharen, D., Mallet, A., & Chandran, B. D. G. 2015, *ApJL*, 801, L18
 Martinović, M. M., Klein, K. G., & Bourouaine, S. 2019, *ApJ*, 879, 43
 Matthaeus, W. H., Dasso, S., Weygand, J. M., Kivelson, M. G., & Osman, K. T. 2010, *ApJL*, 721, L10
 Matthaeus, W. H., Weygand, J. M., & Dasso, S. 2016, *PhRvL*, 116, 245101
 Narita, Y. 2017, *NPGeo*, 24, 203
 Narita, Y., Glassmeier, K.-H., Motschmann, U., & Wilczek, M. 2013, *EP&S*, 65, 5
 Podesta, J. J. 2009, *ApJ*, 698, 986
 Servidio, S., Carbone, V., Dmitruk, P., & Matthaeus, W. H. 2011, *EL*, 96, 55003
 Taylor, G. I. 1938, *RSPSA*, 164, 476
 Vech, D., Klein, K. G., & Kasper, J. C. 2017, *ApJL*, 850, L11
 Weygand, J. M., Matthaeus, W. H., Kivelson, M. G., & Dasso, S. 2013, *JGRA*, 118, 3995